

TJ50.5 INVESTIGATING CONSISTENCY between VIIRS and MODIS over THE OCEANS: THE SENSOR/ENVIRONMENTAL DATA RECORDS

Nima Pahlevan¹, Zhongping Lee¹, Robert Arnone², Adam Lawson³

¹Department of Environmental and Ocean Sciences, University of Massachusetts Boston, Boston, MA 02125

²Department of Marine Science, University of Southern Mississippi, Stennis Space Center, MS 39529

³Naval Research Laboratory, Stennis Space Center, MS 39529

Abstract

The Visible Infrared Imaging Radiometer Suite (VIIRS) onboard the Suomi National Polar-orbiting Operational Environmental Satellite System (NPOESS) Preparatory Project (NPP) (Suomi-NPP) was launched in October 2011 to continue monitoring the globe in a similar fashion as the heritage sensors, such as the MODerate resolution Imaging Spectroradiometer (MODIS). This paper examines the consistency of the products derived from the VIIRS and MODIS (aboard Aqua) observations over open ocean waters. In this cross-comparison, the VIIRS sensor data records (SDR) along with its ocean color products (derived from the standard processing scheme) are temporally analyzed against the corresponding MODIS products.

1. INTRODUCTION

The Suomi-NPP carries the Visible Infrared Imaging Radiometer Suite (VIIRS), which measures the surface reflected/emitted light in 22 spectral channels with ~370m and ~740m ground sampling distance (GSD) at nadir angles along track (Puschell et al. 2003). The Suomi-NPP is an afternoon satellite (part of the A-Train constellation) (Voiland 2010) placed in a near-circular orbit with an average altitude of 833km. The VIIRS instrument is comprised of a rotating telescope sweeping across track (± 56.26 degrees) covering ~3000 km in swath (larger than that of MODIS) (Wu; Xiong 2012). The optical design of VIIRS includes a half-angle mirror (HAM), which rotates in phase (but at half rate) with the telescope. A combination of rotations of the telescope and the HAM, which minimizes instrument polarization effects, forms the scanning pattern across the swath (Hammann; Puschell 2009). Similar to the MODIS design, VIIRS has three focal planes, namely, the visible-near-infrared (VNIR), the short-wave-infrared (SWIR) grouped with the mid-wave-infrared (MWIR), and the long-wave-infrared (LWIR). The VNIR focal plane has 16 and 32 detectors laid out along track for moderate resolution (M) and imagery (I) bands, respectively. One of the primary missions of VIIRS is the continuity in providing the science

community with the global Environmental Data Records (EDRs) over oceanic waters to enable assess climatology, global warming, and net primary production (NPP). In order to deliver observations consistent with the existing ocean color products obtained from MODIS and Sea-viewing Wide Field-of-view Sensor (SeaWiFS), it is crucial to characterize the in-orbit calibration of the VIIRS instrument (Gordon 1990). It is well recognized that small calibration uncertainties may result in unacceptable errors in the retrieval of ocean color (OC) products, such as concentrations of chlorophyll-a (CHL) and inherent optical properties (IOPs) of oceanic waters. In addition to regular monitoring of the instrument behavior, there is always a need to validate the products derived from VIIRS. Such efforts aid in identifying issues in the processing chain, i.e., atmospheric correction (ACO) or IOP retrieval, which leads to critical products, i.e., the remote sensing reflectance (R_{rs}), IOPs, and CHL.

In this paper, we present a trend analysis of the VIIRS products as compared to those of MODIS. These products include sensor data record (SDR) and EDRs pertaining to the OC properties. This analysis complements efforts made by the NOAA STAR/NESDIS, the VIIRS Ocean Science Team (VOST), the OC calibration/validation Team led by NOAA, and the MODIS Characterization Support Team (MCST) at NASA. This cross-validation analysis provides an effective (and inexpensive) post-launch assessment of the VIIRS stability relative to MODIS over oceanic waters.

2. BACKGROUND

2.1 Calibration Techniques

Data continuity/consistency of the EDRs over global oceans requires an instrument with high radiometric fidelity, which satisfies high signal-to-noise ratio (SNR) as well as minimal polarization sensitivity, detector-to-detector inconsistencies, out-of-band response, etc. The

radiometric fidelity of the VIIRS instrument manifests itself as the SDR products. The raw data records (RDR), which is referred to as the raw radiometric measurements of the Earth surface, the measurements made by the calibration devices together with ancillary data (pre-flight characterizations) are utilized to obtain calibrated radiance imagery termed VIIRS SDR. The SDR is the equivalent of the MODIS calibrated radiance (L1B) products in physical units of top-of-atmosphere (TOA) radiance ($W/m^2sr\ nm$). The instrument observations of the solar diffuser (SD), deep space, and the moon coupled with the measurements of the solar

diffuser stability monitor (SDSM) provide a full set of calibration parameters (look-up-table) for each individual detector, spectral channel, and the HAM side to produce SDR (Eplee et al. 2012). This look-up-table (LUT) is updated on a weekly basis to account for degradations in both the SD and the overall performance of the instrument (Eplee et al. 2012) (Wu; Xiong 2012).

Although onboard calibration techniques are necessary during the lifetime of an OC mission, vicarious calibrations (primarily over the Marine Optical Buoy (MOBY)) (Franz et al. 2007) and cross-calibrations (with other sensors) are now common-practice (Kwiatkowska et al. 2008). While vicarious calibration (over one single location in the globe) is limited by the number of clear days and the performance of the forward atmospheric model (Gordon; Wang 1994), in-orbit cross-calibrations with heritage OC sensors, such as MODIS, provide more frequent, near-concurrent dual observations. Needless to say that cross-calibration gives insight only into the relative performance of the instrument, whereas vicarious calibration and onboard calibrations are absolute techniques. That being said, the onboard calibration procedure is also relative to the SD observations and may not provide true absolute radiometric measurements (Eplee et al. 2012). Furthermore, routine vicarious calibrations over the MOBY site are carried out only for the visible bands, i.e., M1- M5 for VIIRS, and it is critical to investigate the VIIRS radiometric responses for the NIR bands (M6 and M7) employed in the ACO procedure (See Table 1). It should be noted that lunar observations and other onboard calibration activities support monitoring of the VIIRS NIR channels. Here, the MODIS instrument aboard Aqua, whose performance has been stable since launch (Xiong et al. 2010), is utilized as the reference system to evaluate the overall performance of the VIIRS instrument. Similar to Suomi-NPP, Aqua is among the A-train constellation (Voiland 2010), however, it is placed in an orbit with a nominal altitude of 705 km. The differences in the orbital configurations

Table 1. The center wavelengths (CW) and the bandwidths of the ocean spectral channels

	VIIRS		MODIS	
	CW	Bandwidth	CW	Bandwidth
M1	412	20	412	15
M2	443	18	443	10
M3	486	20	488	10
M4	555	20	551	10
M5	672	20	667	10
			678	10
M6	746	15	748	10
M7	865	39	869	15

allow for frequent crossing of the two orbits defined as simultaneous nadir overpasses (SNO) along the track (Cao et al. 2004). The SNOs occur very frequently near the Polar regions and less often over low-latitude areas (Cao 2012). However, it is very unlikely that both instruments image ocean waters at SNOs (due to clouds or thick atmospheres). Therefore, it was impossible to make use of the exact SNOs for the present study. Instead, near-simultaneous overpasses (< 15 minutes), where differences in the imaging geometries, i.e., scan/sun angle, are unavoidable, were considered. To overcome the differences in the sun angles, the analysis was conducted for the TOA reflectances products, i.e., ρ_V and ρ_M for VIIRS and MODIS, respectively. In addition, the differences in the spectral response functions, i.e., $RSR(\lambda)$, must be taken into account. Table 1 lists the band configurations associated with the VIIRS M bands and the corresponding MODIS OC channels employed. Although the center wavelengths (CWs) are relatively close (less than 4 nm shift except for M5), the VIIRS spectral bandwidths are broader than those of MODIS OC bands.

2.2 Ocean Color Products

It is also critical to monitor the OC properties (EDR) derived from the SDR to ensure fidelity and continuity of ocean color missions. The EDRs include aerosol, clouds, snow/ice coverage, surface temperature, albedo, vegetation, sea surface temperature (SST), and OC properties, including surface CHL and IOPs. The global monitoring of the OC properties through remote sensing (RS) systems helps to understand global warming patterns, global ocean circulations, ocean clarity, phytoplankton dynamics, coastal/ocean interactions, etc. In contrast to the SST products, which only reveal ocean surface dynamics, the OC products provide information about subsurface (bulk) properties of ocean waters.

The remote sensing reflectance ($R_{rs}(\lambda)$, sr^{-1}) is the primary variable derived from $L_M(\lambda)$ (or $\rho_M(\lambda)$) collected by RS systems. This quantity is critical in the success of an OC mission in that its erroneous retrieval (due to the uncertainties associated with either the imaging device or the ACO procedure) yields incorrect OC products. It is, therefore, crucial to ensure robust estimations of $R_{rs}(\lambda)$ from which IOPs and CHL are drawn. This is, in particular, of interest for a long-term, consistent monitoring of ocean properties to study global climate trends. To evaluate the product quality associated with the Suomi-NPP mission, the VIIRS-derived $R_{rs}(\lambda)$ should be (ideally) compared against *in situ* measurements, which require significant resources, time, and costs. Moreover, such validations must be carried out in clear atmospheric conditions to truly represent a “match-up” under the satellite overpass. In this paper, however, $R_{rs}(\lambda)$ and the associated IOPs and CHL products (from VIIRS) are assessed with the MODIS-derived products. Monitoring the quality of the OC products not only validates the operations of the relevant algorithms but also it serves as a validating technique for the in-orbit cross-comparisons (TOA) presented in this study (Section 4.2.1).

3. CROSS-VALIDATION APPROACH

In this section, the methodology used to compare VIIRS-derived products with the MODIS-derived L1B/surface products is described. While SDR comparisons are referred to as TOA analysis, surface-level comparisons are used to refer to the EDR analysis. For the SDR trending study, 40 scene pairs acquired in March-October 2012 were analyzed. For the same period, nearly half of the scene pairs (identical sense as in the SDR study) at the EDR level were investigated for studying the trends in R_{rs} , CHL, and IOPs.

3.1 Top-of-atmosphere (TOA)

For the evaluation of the TOA radiance, the methodology described in (Pahlevan; Schott 2012) was modified to suit the VIIRS-MODIS cross-calibration. Briefly, strict criteria applied for $\rho_V(865)$ and $\rho_M(869)$ were defined to mask out clouds and turbid atmospheric conditions. In order to avoid uncertainties in the atmospheric conditions at large scan angles, it was decided to limit the cross-comparisons within the near-nadir angles, i.e., $< \pm 10^\circ$. To avoid spatial heterogeneity (due to cloud shadows or aerosols), the coefficient of variation, i.e., $CV(\%)$, associated with $\rho_V(865)$ computed for local areas of 3×3 was further scrutinized. The areas with $< 1\%$ spatial variability were flagged as candidate areas for the cross-comparison. The VIIRS flagged areas were run against the

corresponding MODIS dataset, which had already undergone thresholding using the CV calculated for $\rho_M(936)$, $\rho_M(940)$, and $\rho_M(1375)$. The temporal consistency in the atmospheric conditions between the overpasses was controlled by calculating the ratio of $\rho_V(1240)/\rho_M(1240)$, where $\rho_V(1240)$ is the VIIRS M8 channel and $\rho_M(1240)$ represents the MODIS aggregated land band at 1240 nm. The ratio was allowed to vary within $\pm 1\%$. Further conditions included restricting the differences in the scan angles, i.e., $\Delta\alpha < 5^\circ$, while ensuring that the viewing azimuth angles have identical signs (both instruments viewing either east or west when ascending in their orbits). The corresponding areas (locally averaged) are then compared by calculating the percent differences (PD) as follow

$$PD(\lambda)_N = (\rho_V(\lambda) - \rho_M(\lambda)) / \rho_M(\lambda) \quad (1)$$

where $PD(\lambda)_N$ is expressed in (%). While λ stands for the VNIR bands, i.e., M1–M7, N is the number of corresponding areas that $PD(\lambda)$ are averaged over. Note that the number of corresponding areas (N) ranged from three to 10 depending on how strictly VIIRS scenes were initially masked out. The next step is to account for the differences in $RSR(\lambda)$ and imaging geometries. This is achieved by creating LUTs formed by varying upper-air atmospheres and aerosol conditions. The LUT was generated through forward MODTRAN simulations (Berk et al. 1989) to match $L_V(\lambda)$ and $L_M(\lambda)$, i.e., the measured TOA radiances associated with MODIS and VIIRS, respectively. Table 2 contains MODTRAN configurations for the LUT generation for each scene pair. The TOA radiances ($W/m^2 sr nm$) are then passed through $RSR(\lambda)$ corresponding to each instrument:

$$L_{eff}(\lambda_0) = \frac{\int_{bandpass} L(\lambda) RSR(\lambda) d\lambda}{\int_{bandpass} RSR(\lambda) d\lambda} \quad (2)$$

where $L_{eff}(\lambda_0)$ stands for the effective TOA radiance at the CW λ_0 . The match was found by comparing the modeled TOA radiances (resampled to the MODIS $RSR(\lambda)$) to those collected by MODIS on a per-band basis (same results would be achieved if comparisons are made for VIIRS). It should be noted that this process aims only at predicting TOA radiances similar to those observed, which leads to estimating the differences due to the discrepancies in $RSR(\lambda)$ and imaging geometries, i.e., H and α , which stand for altitude and scan angle. The output of this process is a ratio factor (α) found to compensate for such differences:

$$\alpha(\lambda) = \frac{L_V^p(\lambda)}{L_M^p(\lambda)} \quad (3)$$

where $L_V^p(\lambda)$ and $L_M^p(\lambda)$ correspond to the modeled VIIRS and MODIS TOA radiances, which were found to match the observed values. The measured $L_M(\lambda)$ is then adjusted by multiplying by (α) , which is then converted to $\rho_M(\lambda)$ (Schott 2007). The adjustment forces the MODIS measurements to appear to have been collected from an identical platform/instrument (Suomi-NPP/VIIRS) at the same scan angle. The (α) parameter found for all the scene pairs ranges from 0.97 to 1.06 depending on the spectral channels and scan angles. A complete description of the uncertainties associated with this adjustment is given in (Pahlevan; Schott 2012).

3.2 Surface level

The approach followed for the cross-validation of EDRs is similar to that described in Section 3.1. The EDR analysis was performed for the scene pairs studied in Section 3.1, however, only half of them were utilized. Since radiometric uncertainties associated with the instrument, i.e., $\Delta L(\lambda)$, are propagated to the derived $R_{rs}(\lambda)$, this comparison serves as a validating method for the cross-calibration technique applied (Section 3.1). As a part of the OC calibration/validation activities, it is desired to analyze the standard VIIRS products processed via the Interface Data Processing Segment (IDPS) established by the Joint Polar Satellite System (JPSS) at NOAA. The standard atmospheric correction

Table 2. The MODTRAN configuration for the LUT generation

	VIIRS	MODIS
Height (km)	$H_1 = 833$	$H_2 = 705$
Angle	α_1	α_2
Aerosol Type	Maritime	
Time	Mean overpass time	
Spectral range/resolution	(400-1500nm)/1nm	
Geographic location	mean lat/long	
Day of year (DOY)	Variable	

(Gordon; Wang 1994) is implemented in IDPS as a primary component of the OC processing scheme. This is followed by the retrieval of the IOPs, including total absorption (Abs) and backscattering (Sct) coefficients, and CHL. The MODIS products, on the other hand, were obtained from the Naval Research Laboratory (NRL). The NRL processing system uses a modified Gordon-Wang model (a broader range of aerosol models) to generate $R_{rs}(\lambda)$, CHL, IOPs (equivalent of IDPS-processed IOPs), and aerosol radiances.

Similar to the TOA comparisons, the cross-comparisons were spatially restricted to the near-nadir angles, i.e., $< \pm 10^\circ$. The MODIS scenes were first searched for areas with minimum local variability (3×3 boxes) and then were masked out based on a threshold, i.e., T . The candidate areas were selected by thresholding $R_{rs}(412)$ products, i.e., $T < 1\%$ for the CV calculated in each box.

In a similar fashion, the corresponding areas in the VIIRS products were examined for their variability and, if sufficiently small, were utilized in the subsequent cross-comparisons. The disparity between the two products was computed using Eq.1 by replacing the TOA reflectances (ρ) with R_{rs} and IOPs. For analyzing the CHL products, it was decided to generate scatterplots to qualitatively investigate the consistency between all scene pairs. Although the TOA trends in M1-M7 are studied, it was decided that the EDR trends for M1-M4 be considered in this section. This is because the MODIS EDR retrieval algorithms for the red bands are under development during this study. For this study, the discrepancies in the band configurations for M3 and M4 (VIIRS) versus the corresponding bands of MODIS were assumed negligible in the EDR analysis. In addition to the band-to-band cross-comparisons, locally derived CVs calculated for all of the areas of minimum variability (VIIRS and MODIS) were evaluated to examine whether striping and banding effects (differences in the responses due to different mirror sides) are properly accounted for in the VIIRS OC processing chain.

4. RESULTS

4.1 SDR Trends

A total of 41 scenes over various oceanic/open waters, including Indian Ocean, North/South Atlantic, South Pacific, Barents Sea, and Southern Ocean, during solar summers/winters are included in the analysis. The diverse set of samples enabled a robust performance analysis (of the VIIRS instrument) over a large signal range. The scene pairs are chosen such that at least one cross-comparison per week is made (March-October 2012). Fig. 1 & Fig.2 illustrates the trend analysis (Eq. 1) for the visible and the NIR bands, respectively. The period of study is from the day of year (DOY) 60 through 305. The red dashed lines indicate uncertainty bounds, i.e., $\pm 2\%$, within which the disparity between the two sensors are assumed negligible. The boxes show two timeframes when large differences in the relative responses are observed. It should also be noted that the differences in the imaging geometries and $RSR(\lambda)$ have been accounted for (Section 3.1.). During

the early days (DOY<120), the VIIRS responses within $\lambda < 555$ (Fig. 1) is, on average, consistent with those of MODIS ($\Delta L \leq \pm 2\%$). However, during this timeframe, $\rho_V(\lambda > 486)$ are found to be +3.1% and +4%, on average, higher than the MODIS observations at $\lambda \approx 555$ and $\lambda \approx 672$, respectively. While the VIIRS radiometric response at $\lambda \approx 746$ is, on average, in a good agreement with that of MODIS ($\Delta L \approx \pm 0.4\%$), the recorded signal at $\lambda \approx 865$ was found to be 5.1%, on average, larger than the corresponding MODIS signal in DOY<120 (Fig. 2). It can be seen in Fig. 2 that the trends in the NIR bands remains more stable than that of the visible bands over the entire period.

$1.8 < L(865) < 3$ ($W/m^2sr\ nm$), over the oceans are, in general, very low; therefore, changes in the SD trends may not be revealed. The relative discrepancies in the NIR bands for DOY>120 are, on average, -2.9% and +3.4% for M6 and M7, respectively. The biases found for these bands may lead to erroneous choice of aerosol models and, as a result, incorrect ACO. For the same period, VIIRS exhibits -1.6%, -5%, -3.7%, +0.2%, and +1.5% differences for M1, M2, M3, M4, and M5, respectively. These discrepancies when compared to the differences during DOY<120 indicate a significant decrease in the overall VIIRS radiometric response after DOY=120. After DOY>200, however, $\rho_V(\lambda < 700)$

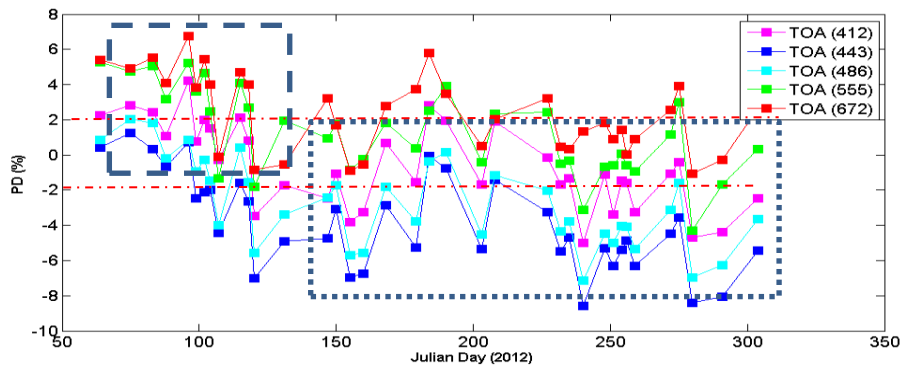


Fig. 1. The percent difference (PD) trending found for the visible bands at TOA. The VIIRS radiometric responses are larger or equal for DOY<120 but smaller for DOY>120. The red rash lines indicate $\pm 2\%$.

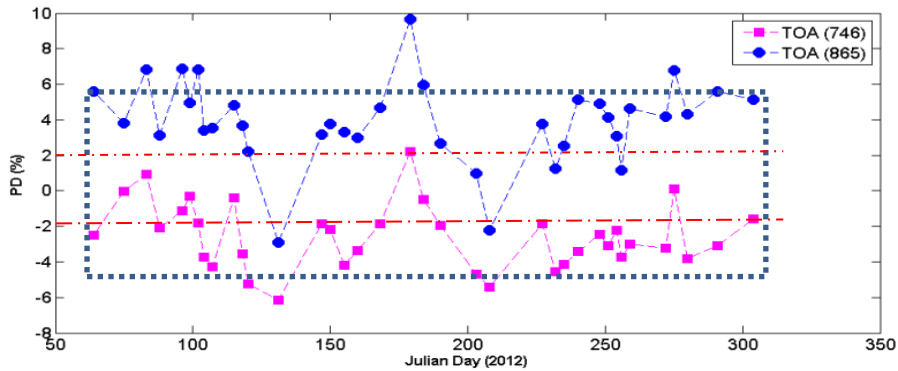


Fig. 2. The percent difference (PD) trending found for the NIR bands at TOA. The trending is more stable than that in the visible bands over the entire period.

This is perhaps due to the fact that the degradations in the Bi-directional Reflectance Distribution Function (BRDF) of the SD are less apparent in the NIR responses than in the visible bands (Fig. 1) (Eplee et al. 2012). Furthermore, the radiometric sensitivity of the optical instruments within the NIR channels at small signal levels, i.e., $4.2 < L(746) < 5.8$ and

reaches its minimum value. Also, the offsets observed for $\rho_V(\lambda < 672)$ during DOY>200 will impact the retrieval of CHL (Section 4.2.3). The discontinuity around DOY=120 comes from the updates of the VIIRS SD screen transmittance, which were derived on-orbit after instrument yaw maneuvers (Wu 2013).

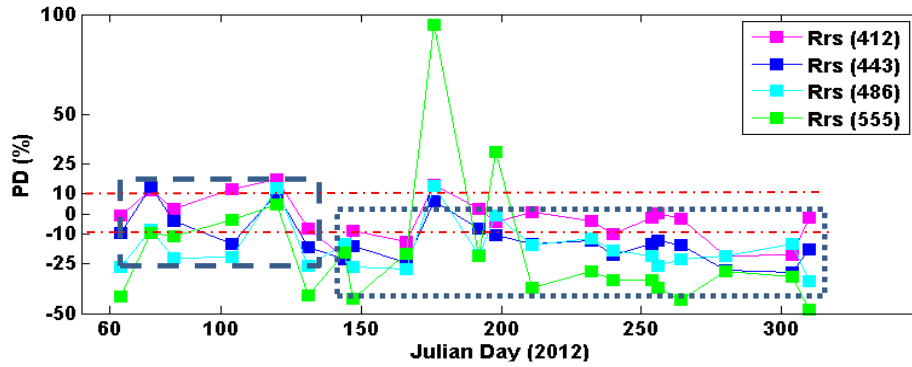


Fig. 3. The PD trending associated with R_{rs} . The temporal variability which is consistent with the trends in the TOA study (Fig. 1). The boxes indicate the two timeframes at which a notable change the relative differences is observed.

The average temporal variability was found to be $\sigma \approx 2.3\% \pm 0.2$ for all bands. The variability is likely due to a) the changes in the VIIRS LUT (F-factor) corresponding to the degradations in the SD and b) uncertainties associated with the TOA cross-comparisons (Pahlevan; Schott 2012). The large-scale variations, e.g. the peak at DOY~180 in Fig. 1 and Fig. 2, can be linked to the former, whereas the small-scale changes (noise) are thought to be associated with the latter. In other words, if the temporal trends were linearly filtered the smoothed sequence would solely correspond to large scale variations. It should be noted that all of the discussions here are based on the assumption that the Aqua (MODIS) radiometric response has remained stable during March-October 2012.

Inter-channel cross-correlations between the PDs can also lead to further quantitative information regarding the spectrally varying SD degradations (Table 3). The cross-correlations represent how the temporal variations are correlated among different channels at the TOA radiances. From Fig. 1 and Fig. 2, it can be inferred that the trends in the visible bands are correlated, while the NIR trending is not correlated with the trending in the visible bands.

Table 3. Inter-band cross-correlations

	M1	M2	M3	M4	M5	M6	M7
M1	1						
M2	0.97	1					
M3	0.96	0.98	1				
M4	0.86	0.90	0.94	1			
M5	0.86	0.85	0.88	0.85	1		
M6	0.56	0.50	0.57	0.48	0.74	1	
M7	0.24	0.21	0.26	0.25	0.58	0.72	1

Table 3 gives a more quantitative detail for the inter-band correlations. Although M1 is well correlated with M2 and M3 ($r^2 > 0.95$), there is a weak correlation between M1 and M4-M5. Note that any uncertainty due to the inconsistencies in the atmospheric conditions (between the overpasses) contributes the most in the NIR analysis.

4.2 Ocean Color EDR Trends

4.2.1 Remote sensing reflectance/IOPs

Figure 3 illustrates the temporal analysis for R_{rs} and IOPs. The red dashed lines indicate uncertainty bounds, i.e., $\pm 10\%$, within which the disparity between the two sensors are assumed negligible. The boxes show the two timeframes when large differences in the relative R_{rs} are observed. Overall, the R_{rs} time series indicates notable anomalies in the PDs during the early days, i.e., DOY < 120. While the VIIRS-derived R_{rs} is slightly larger than that of MODIS for $R_{rs}(412)$ and $R_{rs}(443)$ during DOY < 120, the VIIRS-derived R_{rs} products are nearly always lower than that of MODIS for the other visible bands during the entire period (Fig. 3). The average discrepancy in DOY < 120 is equivalent to +9%, -1%, -13%, and -12% for the visible bands, respectively. For DOY > 120, the trend remains relatively stable for all of the bands except a peak at DOY~180. During this timeframe, the average differences are -7%, -18%, -21%, and -32% for M1, M2, M3, and M4, respectively. The peak difference observed around DOY=180 for $R_{rs}(555)$ (as well as for other bands) is consistent with that observed in Fig. 1.

Since, for most of the ocean waters, small disparities, i.e., <10%, associated with R_{rs} ($\lambda < 672$) does not significantly impact the IOP retrievals, it is expected that the IOP products derived from VIIRS and MODIS within $\lambda < 672$ be consistent. However, both total absorption (+27%, +41%, +35%, and +37% for M1-

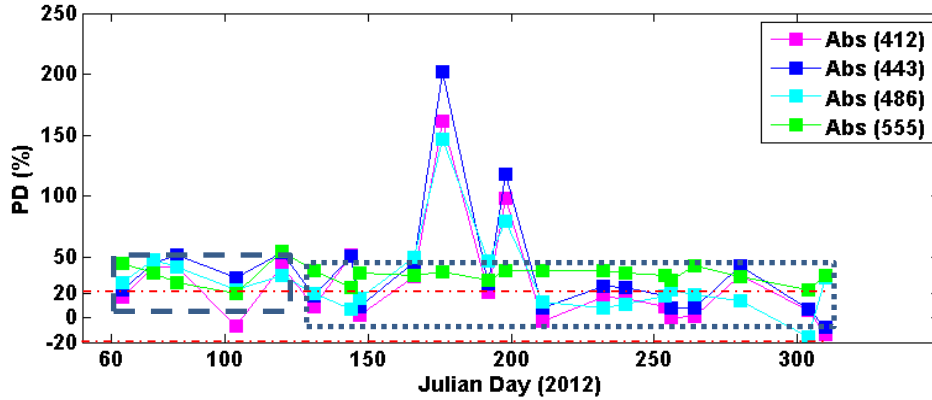


Fig. 4. The PD trending associated with absorption (Abs) properties (M1-M4) of oceanic waters. The red dashed line indicates 20% uncertainty bounds.

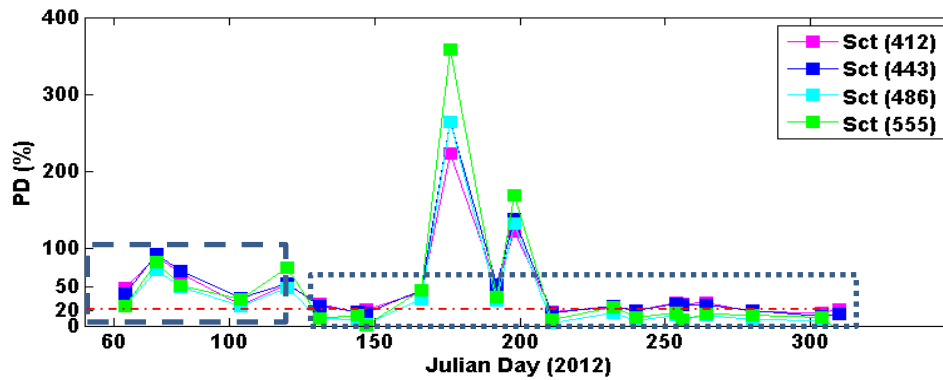


Fig. 5. The PD trending associated with backscattering (Sct) properties (M1-M4) of oceanic waters. The red dashed line indicates 20% uncertainty bounds.

M4, respectively) and backscattering (+57%, +59%, +45%, and +54% for M1-M4, respectively) coefficients derived from the VIIRS R_{rs} using the standard processing algorithms (IDPS) are overestimated for $DOY < 120$ (Fig. 4 and Fig. 5). This is, in part, due to the discrepancies in the algorithms applied for the IOP retrieval. The NRL processing system uses Quasi-Analytical Algorithm (QAA) (Lee et al. 2002), while the semi-analytical Carder method (Carder et al. 2003) is utilized in IDPS. Similar trends observed for R_{rs} were also seen for the IOP temporal variations. The exception is the total absorption coefficients at 555nm, i.e., Abs(555), where the temporal variability is relatively stable. It should be further emphasized that the backscattering coefficients exhibit the largest discrepancies against the corresponding MODIS-derived coefficients, (Fig. 5), when compared to the differences in the absorption coefficients.

4.2.2 Spatial variability

In order to analyze whether striping and banding effects are properly removed in the VIIRS OC

processing chain, the spatial variability associated with R_{rs} and IOP products derived from VIIRS and MODIS is evaluated. Due to the nature of oceanic waters, spatial variability associated with the sample areas, over which cross-comparisons are made, is expected. In this section, it is assumed that the variability in the MODIS-derived products corresponds to bodies of water and is considered as a reference to investigate the consistencies with the VIIRS products. Fig. 6 shows the time-averaged CVs computed for the areas used for the previous analyses (Section 4.2.1). Although the VIIRS-derived variability in R_{rs} (412), R_{rs} (443), R_{rs} (486), and R_{rs} (555), is very similar to that of MODIS, the VIIRS-derived absorption (Abs-V) and backscattering (Sct-V) coefficients (for the same bands) represent slightly more variability than those associated with MODIS, i.e., 14% versus 10%, on average. The exceptions are the VIIRS-derived Abs(555) and Abs(672), where the corresponding spatial variability is ~1.1% and 0.8%, respectively.

This is in contrary with ~5% and ~10% variability obtained for the MODIS products, i.e., Abs(555). While

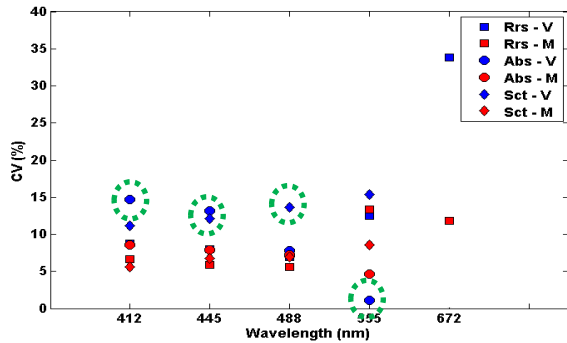


Fig. 6. The coefficient of variations (CVs) calculated and averaged for all the sampled areas used in the analysis presented in Section 4.2.1. V and M correspond to statistics derived from VIIRS and MODIS, respectively.

a minimum variability (due to natural waters) is expected, near-zero variability for Abs (555) may be related to the weak performance of the IOP retrieval algorithm. This requires further investigations of the IOP retrievals (over well-known regions like South/North Pacific/Atlantic Gyres) for both VIIRS and MODIS products. On the other hand, the variability obtained for VIIRS-derived backscattering coefficients (Sct) are approximately twice as large as those of MODIS over all the bands. The largest discrepancy between the products is obtained for $R_{rs}(672)$, where the VIIRS-derived CV is more than three times greater than that of MODIS. The large variability is likely associated with the striping and banding effects and needs further analysis.

4.2.3 Chlorophyll-a

Figure 7 illustrates scatterplots of CHL products derived from VIIRS and MODIS. The comparisons were made for the two periods, i.e., DOY<120 and DOY>120. The data points were extracted from all of the ROIs (over 41 scenes) meeting the criteria defined in Section 3.2. For the DOY<120 timeframe, the CHL retrieval is shown to exhibit relative consistency with that obtained

from MODIS. However, the VIIRS-derived products are slightly overestimated (Fig. 7a). It should be noted that a few outliers (< 1% of total) shown in Fig. 7a is insignificant in the analysis. It is clearly seen in Fig. 7b that the correlation between the CHL products of VIIRS and MODIS (DOY>120) is not strong, i.e., $r^2 < 0.79$ and RMSE= $0.17 \mu\text{g}/\text{l}$. While, in general, the VIIRS-derived CHL values are higher, the MODIS-derived values represent smaller variability ($\sigma_M = 0.015$ versus $\sigma_V = 0.037$).

5. CONCLUSIONS

In this paper, the VIIRS-derived products over the oceans, including SDR and EDR, were compared against the corresponding products obtained from MODIS for the period of March through October 2012. The system-level cross-comparison between the two instruments indicates a relative consistency in the short visible bands for DOY< 120. However, the consistency decreases after DOY=120, which results from lower radiometric responses of VIIRS across all of the visible bands. Although anomalies were observed in the SDR trends for DOY>120, it is believed that the lower responses of VIIRS come from the SD characterization and its BRDF trends. In contrast, the differences in the NIR bands were found to be relatively stable, i.e., -2.9% and +3.5% bias, on average, except a peak around DOY=180. It is critical to study how such radiometric uncertainties in the NIR bands propagate through the OC products. The cross-comparisons were also made for the surface-level products, where R_{rs} , IOPs, and CHL products are assessed. Overall, the trends found for the EDRs were in agreement with the SDR trends. However, during DOY<120, when VIIRS-MODIS discrepancies at TOA are minimal, relatively large variability in the trends is observed. In a similar fashion, one would expect that the IOPs be consistent during DOY<120.

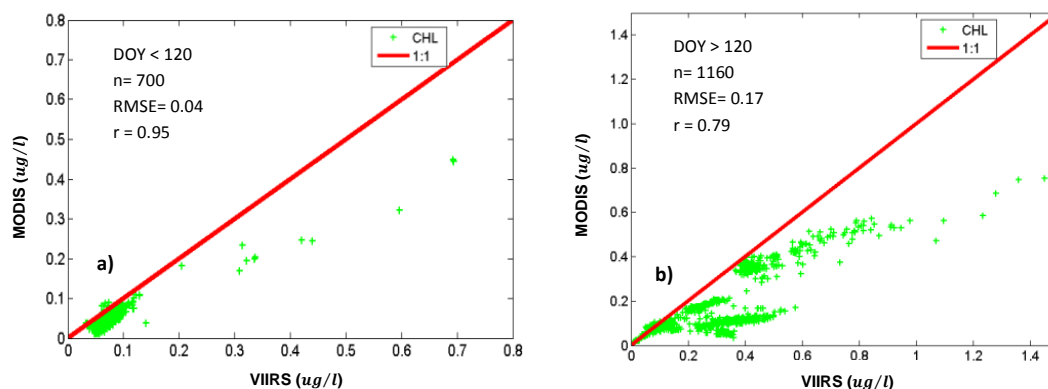


Fig. 7. The scatterplots of the CHL products for a) DOY<120 and b) DOY>120. The red line represents the 1:1 slope.

Nevertheless, more than 35% and 45% disparity, on average, were found in the absorption and scattering coefficients, respectively, for DOY<120. However, the discrepancies in the IOPs to some extent can be attributed to the differences in the retrieval algorithms. Further studies over optically stable sites (like Gyres) are required to make valid conclusions on the performance of the retrieval algorithms. In addition, the differences in the spatial variability between the IOPs derived from VIIRS and MODIS reinforce the need for further analysis. The primary reason is that the MODIS and VIIRS processing systems apply different algorithms thereby making it difficult to make fair comparisons.

ACKNOWLEDGEMENTS

The authors would like to thank the ocean color calibration/validation team, including Dr. Bruce Guenther and Patty Pratt, for providing comments/feedback on the progress of this study. We also would like to appreciate the help from Sherwin Lander and Jennifer Bowers with NRL. Financial support provided by NOAA STAR program is greatly appreciated.

References

Berk, A., L. Bernstein, and D. C. Robertson, 1989: MODTRAN: a moderate resolution model for LOWTRAN 7.

Cao, C.: National Calibration Center. [Available online at <https://cs.star.nesdis.noaa.gov/NCC/SNOPredictions>.]

Cao, C., M. Weinreb, and H. Xu, 2004: Predicting Simultaneous Nadir Overpasses among Polar-Orbiting Meteorological Satellites for the Intersatellite Calibration of Radiometers. *Journal of Atmospheric and Oceanic Technology*, **21**, 537-542.

Carder, L., R. Chen, F., Z. Lee, Ping, S. K. Hawes, and J. Cannizaro, P., 2003: MODIS Ocean Science Team Algorithm Theoretical Basis Document, 67 pp.

Eplee, R. E., and Coauthors, 2012: VIIRS on-orbit calibration for ocean color data processing, 85101G-85101G.

Franz, B. A., S. W. Bailey, P. J. Werdell, and C. R. McClain, 2007: Sensor-independent approach to the vicarious calibration of satellite ocean color radiometry. *Appl. Opt.*, **46**, 5068-5082.

Gordon, H. R., 1990: Radiometric considerations for ocean color remote sensors. *Appl. Optics*, **29**, 3228-3236.

Gordon, H. R., and M. Wang, 1994: Retrieval of water-leaving radiance and aerosol optical thickness over the oceans with SeaWiFS: a preliminary algorithm. *Appl. Opt.*, **33**, 443-452.

Hammann, M. G., and J. J. Puschell, 2009: SeaWiFS-2: an ocean color data continuity mission to address climate change, 745804-745804.

Kwiatkowska, E. J., B. A. Franz, G. Meister, C. R. McClain, and X. X. Xiong, 2008: Cross calibration of ocean-color bands from Moderate Resolution Imaging Spectroradiometer on Terra platform. *Appl. Optics*, **47**, 6796-6810.

Lee, Z. P., K. L. Carder, and R. A. Arnone, 2002: Deriving inherent optical properties from water color: a multiband quasi-analytical algorithm for optically deep waters. *Appl. Optics*, **41**, 5755-5772.

Pahlevan, N., and J. R. Schott, 2012: Characterizing the relative calibration of Landsat-7 (ETM+) visible bands with Terra (MODIS) over clear waters: The implications for monitoring water resources. *Remote Sensing of Environment*, **125**, 167-180.

Puschell, J., and Coauthors: NPOESS Visible Infrared Imaging Radiometer Suite (VIIRS) Sensor Design and Performance. [Available online at <http://cimss.ssec.wisc.edu/itwg/itsc/itsc13/session10/Puschell%20VIIRS%20Sensor%20Performance%20ITSC%20FINAL.pdf>.]

Schott, J. R., 2007: *Remote Sensing The Image Chain Approach*. 2nd ed. Oxford University Press, 666 pp.

Voiland, A.: Introducing the A-Train. [Available online at http://www.nasa.gov/mission_pages/a-train/a-train.html.]

Wu, A., and X. Xiong, 2012: NPP VIIRS and Aqua MODIS RSB comparison using observations from simultaneous nadir overpasses (SNO), 85100P-85100P.

Wu, A. S., 2013: VIIRS SDR Report

Xiong, X. X., J. Q. Sun, X. B. Xie, W. L. Barnes, and V. V. Salomonson, 2010: On-Orbit Calibration and Performance of Aqua MODIS Reflective Solar Bands. *IEEE Trans. Geosci. Remote Sensing*, **48**, 535-546.